Fourier-Space Image Restoration

Ronald R. Parenti

■ Computational restoration techniques are frequently applied to two-dimensional images when the propagation medium or noise in the sensing apparatus significantly corrupts the recorded image data. Deconvolution processes are among the oldest and best understood of these techniques, although nonlinear and iterative computational methods can provide superior performance when real-time data processing is not a requirement. For many practical problems, however, Fourier deconvolution is the method of choice, because acceptable results can usually be obtained with a minimum of computational effort. The correction of point-spread-function distortions induced by sparse-aperture receivers is an example of an application for which Fourier deconvolution is particularly well suited.

Sparse-aperture optical telescopes are highly advantageous if the costs associated with the orbital deployment of a filled-aperture receiver are prohibitive. A telescope incorporating a sparse-aperture mirror could be compactly folded to make a small lightweight payload, which could be placed into orbit by a relatively inexpensive launch vehicle. Although the raw imagery produced by a sparse-aperture system would show significant distortions, near-diffraction-limited images can be recovered by using appropriate data processing techniques.

To motivate this investigation, we use a three-petal telescope structure having a 10% fill factor as a model to study the image reconstruction process and its sensitivity to sensor noise. A receiver of this type can produce images comparable to those generated by a filled aperture of the same diameter, provided that an average signal-to-noise ratio on the order of 100 can be maintained over the entire image. The results of this study are promising, and lend strong support to the feasibility of constructing inexpensive, lightweight surveillance satellites employing folded-mirror architectures.

The application of Fourier deconvolution to two-dimensional image processing was pioneered by Robert Nathan, who used this procedure to improve the quality of pictures received from the Ranger and Mariner missions in the mid-1960s [1]. This technique has since been refined by a number of investigators, including J.L. Harris [2], C.W. Helstrom [3], D. Slepian [4], and W.K. Pratt [5]. In 1970 A. Labeyrie [6] proposed a variant of this technique to extract the autocorrelation function of celestial objects from short-exposure astronomical images distorted by atmospheric turbulence; this process is referred to as *speckle interferometry.* Although astronomers have found speckle interferometry to be useful, its applicability is limited to the investigation of objects having relatively simple structures, such as binary stars. The full power of the Fourier deconvolution process can be exploited as a means of reconstructing true two-dimensional images only if instantaneous samples of focal-plane sensor data can be combined with simultaneous measurements (or *a priori* knowledge) of the aperture-plane pupil function. This computational approach has been successfully applied to correct the effects of turbulence without the use of deformable mirrors (see the sidebar entitled "Turbulence-Free Astronomical Imaging").

TURBULENCE-FREE ASTRONOMICAL IMAGING

ATMOSPHERIC TURBULENCE imposes a time-varying phase perturbation on the wavefront of any radiation that propagates through the atmosphere; this effect severely distorts imagery produced by terrestrial telescopes. An adaptive optics system can be used to sense the input wavefront and apply a real-time correction to the wavefront with the aid of a mechanically actuated deformable mirror, as indicated in Figure A [1]. Elimination of the wavefront distortion permits near-diffraction-limited pictures to be formed at the focus of the telescope.

Image compensation can also be performed without the aid of a mechanical phase-correction device by computationally deconvolving the measured wavefront distortion from the digitized imagery. This alternative approach is illustrated in Figure B.

The Fourier deconvolution techniques described in this article have been successfully applied to imagery collected with Lincoln Laboratory's 241-chan-

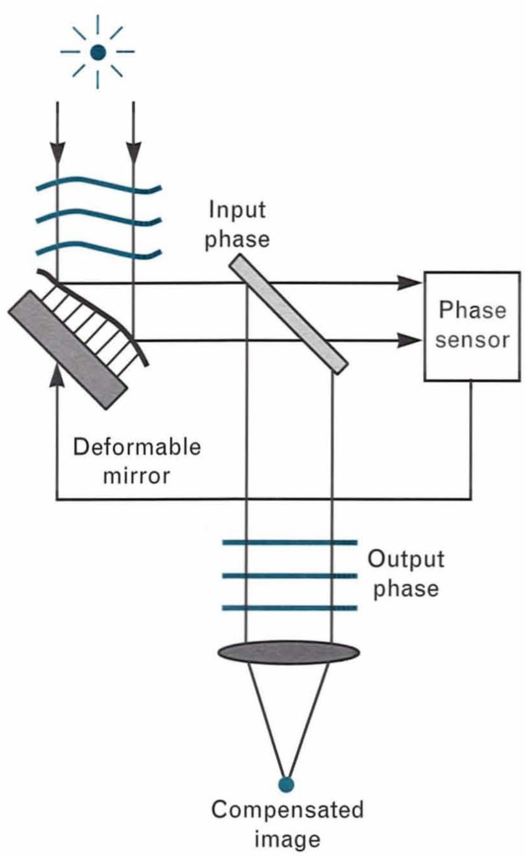

FIGURE A. System architecture for adaptive optics restoration. The phase sensor determines the input wavefront and the deformable mirror is mechanically altered to correct for the distortions in the input wavefront.

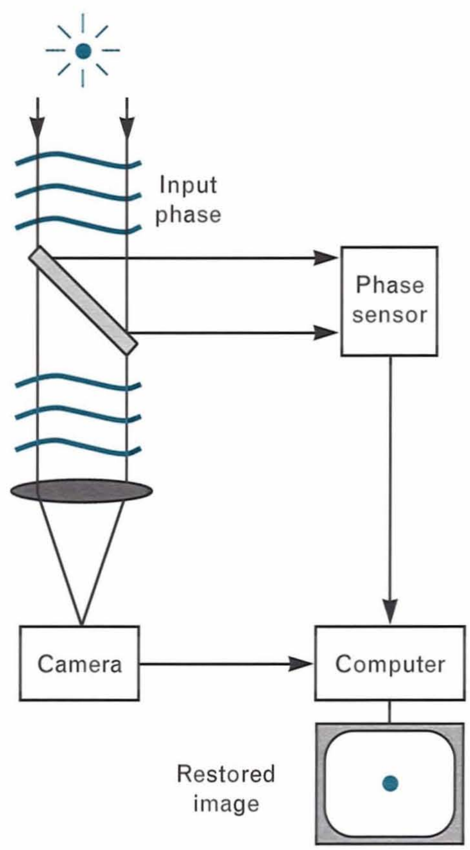

FIGURE B. System architecture for computational image restoration. This system employs no active error-correction hardware, but relies on computationally combining the digitized imagery with measurements of the input wavefront.

nel adaptive optics system [2]. Figure C compares representative image distortion profiles for the star Vega, showing point spread functions of the original distorted image, the image obtained with the adaptive optics system, and the image obtained through computational reconstruction. Although an adaptive optics system always yields superior results under low signal-to-noise conditions, the requisite hardware modifications for computational reconstruction are more easily implemented, particularly in an existing facility where space might be limited.

References
1. D.P. Greenwood and C.A. Primmerman, "Adaptive Optics Research at Lincoln Laboratory," *Linc. Lab. J.* 5, 3 (1992).
2. D.V. Murphy, "Atmospheric-Turbulence Compensation Experiments Using Cooperative Beacons," *Linc. Lab. J.* 5, 25 (1992).

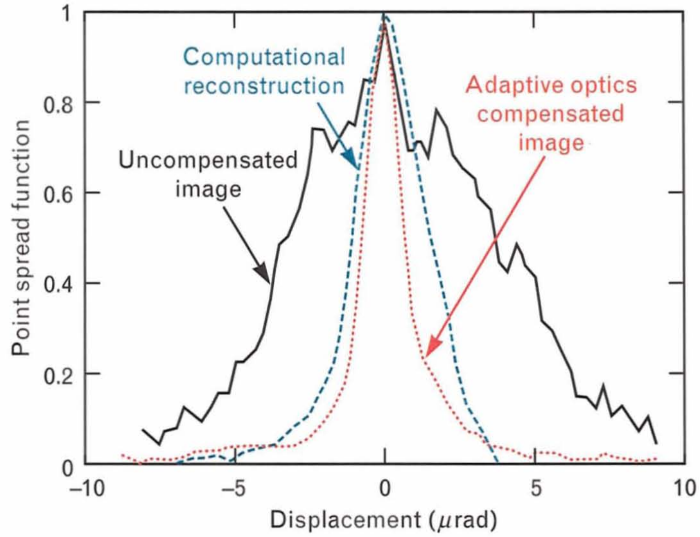

FIGURE C. Experimental data comparing turbulence-compensated point spread functions of the star Vega obtained with a 241-channel adaptive optics system and with Fourier deconvolution. Computational reconstruction techniques are typically somewhat less effective than real-time adaptive optics phase compensation, and in this example the profile of the reconstructed star image is about 50% wider than the profile generated by the adaptive optics system.

The purpose of this article is to demonstrate the effectiveness of Fourier deconvolution for a visible-imaging application in which the optical transfer function can be accurately determined. Specifically, we describe a simulation in which terrain imagery obtained from a Landsat satellite is first processed to replicate the image that would be produced by a highly thinned receiver. The Fourier deconvolution process is then implemented by using the optical transfer function appropriate for the collection aperture. To gauge the practical utility of the technique, we repeated the deconvolution process for a range of signal-to-noise conditions. Finally, we show that the requisite signal-to-noise ratio for faithful reproduction can be achieved for a nominal satellite-surveillance scenario.

Basic Mathematical and Physical Concepts of Image Restoration

The implementation of any data-recovery procedure requires considerable care to avoid mathematical singularities and the introduction of excess noise. To convey an appreciation for these concerns, we first briefly review the derivation of the deconvolution concept as it applies to optical imagery.

The single-element optical system illustrated in Figure 1 incorporates all of the spatial relationships essential to this discussion. The lens is placed at the origin of the coordinate system, with the x-axis and y-axis in the aperture plane, and the object and image planes are located at $z = -R$ and $z = f$, respectively. We assume that the distance R is much longer than the

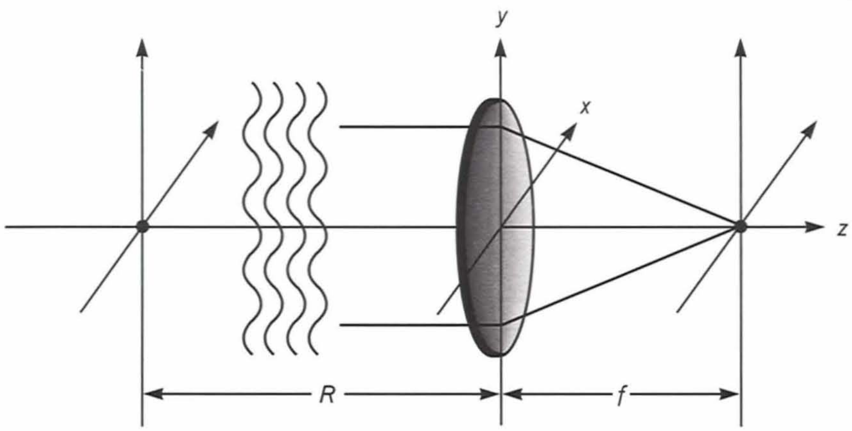

FIGURE 1. Spatial relationship between the object, aperture, and image planes of a simple imaging system. The object is assumed to be separated from the lens by a distance that is much longer than the Fresnel distance D^2/λ, where D and λ represent the aperture diameter and optical wavelength, respectively. The lens is placed at the origin of the coordinate system, and the object and image planes are located at $z = -R$ and $z = f$, respectively.

Fresnel distance D^2/λ, where D and λ represent the aperture diameter and optical wavelength, respectively. For large values of R, the distance f is equal to the focal length of the lens.

For the geometry indicated in Figure 1, the lens is situated in the Fourier plane of both the object and the image. The relationship between the electric field U_a in the aperture plane and the field U_i in the image plane is

$$\begin{aligned} \mathcal{F}\{U_i(x, y)\} &\equiv u_i(f_x, f_y) \\ &= C U_a(\lambda f f_x, \lambda f f_y), \end{aligned} \tag{1}$$

where $\mathcal{F}\{\cdot\}$ represents the Fourier transform and C is a constant. It is clear from this expression that the magnitude of the electric field's spatial frequency at (f_x, f_y) in the image plane is proportional to the magnitude of the field at point $(x/\lambda f, y/\lambda f)$ in the plane of the lens.

A detector placed in the image plane does not directly record the electric field, but rather the square of the field, which is defined as the field intensity I, where

$$I = |U_i|^2 . \tag{2}$$

In an ideal receiver the intensity pattern is equal to the convolution of the aperture's point spread function PSF with the object function O, or

$$I = O \otimes PSF_c ,$$

where the subscript c is used to identify the point spread function of a circular aperture. If some form of optical distortion is introduced at the plane of the lens, the point spread function will include a second component, indicated by the subscript d, which results in a distorted image I', where

$$I' = O \otimes PSF_c \otimes PSF_d .$$

For computational convenience we can represent this relationship as a linear operation in the Fourier domain,

$$\mathcal{F}\{I'\} = \mathcal{F}\{O\} OTF_c \, OTF_d = \mathcal{F}\{I\} OTF_d , \tag{3}$$

which makes use of the fact that the optical transfer function OTF and the point spread function are Fourier transform pairs. This equation forms the basis for the deconvolution operation, in which we attempt to recover the diffraction-limited image I from the corrupted image I'.

If all of the distortion effects are multiplicative in the plane of the aperture, as suggested by Equation 3, then it is possible to compute the optical transfer function from the pupil function P, which describes the shape and phase-delay characteristics of the receiver's primary collector. As the light passes through the aperture plane, a distorted field U'_a is generated, where

$$U'_a = PU_a \,.$$

When this expression is combined with Equations 1 and 2, the following relationship is developed:

$$\mathcal{F}\{I'\} = C^2\left[P(\lambda f f_x, \lambda f f_y)U_a(\lambda f f_x, \lambda f f_y)\right] \otimes \left[P(\lambda f f_x, \lambda f f_y)U_a(\lambda f f_x, \lambda f f_y)\right]^* .$$

For incoherent illumination, this expression is equal to the product of the convolutions of the pupil function and the aperture-plane electric field [7]; i.e.,

$$\mathcal{F}\{I'\} = C^2\left[U_a(\lambda f f_x, \lambda f f_y) \otimes U_a^*(\lambda f f_x, \lambda f f_y)\right] \left[P(\lambda f f_x, \lambda f f_y) \otimes P^*(\lambda f f_x, \lambda f f_y)\right].$$

This form demonstrates that the system's optical transfer function is proportional to the convolution of the pupil function. By convention, the optical transfer function is normalized to unity; the specific form of the calculation is

$$OTF(f_x, f_y) = \frac{\int\limits_{-\infty}^{\infty}\int\limits_{-\infty}^{\infty} P(x, y)P^*(x - \lambda f f_x, y - \lambda f f_y)\, dx\, dy}{\int\limits_{-\infty}^{\infty}\int\limits_{-\infty}^{\infty} |P(x, y)|^2\, dx\, dy} . \tag{4}$$

We can demonstrate the relationship between the optical transfer function and the point spread function by computing these functions for a circular collector. For a lens of diameter D, the pupil function P is described by the circle function of the radial parameter r,

$$P_c(r) = \begin{cases} 1 & r \le D \\ 0 & r > D \end{cases} ,$$

where

$$r = \sqrt{x^2 + y^2} \,.$$

For this symmetry we can define the one-dimensional spatial frequency

$$f_r = \sqrt{f_x^2 + f_y^2} \,.$$

From the convolution of the circle function we obtain the following expression for the optical transfer function of f_r,

$$OTF_c(f_r) = \frac{2}{\pi}\left[\cos^{-1}\left(\frac{|f_r|}{f_0}\right) - \frac{|f_r|}{f_0}\sqrt{1 - \left(\frac{|f_r|}{f_0}\right)^2}\,\right] \quad \text{for } |f_r| \le f_0 ,$$

and

$$OTF_c(f_r) = 0 \quad \text{for } |f_r| > f_0 \,.$$

The cutoff frequency f_0 for a circular aperture is equal to $D/\lambda f$, as illustrated in Figure 2. The point spread function is computed by using the Hankel transform; the result is the familiar Airy pattern,

$$PSF_c(r) = \frac{\pi D^2}{4(\lambda f)^2}\left[2\,\frac{J_1(\pi D r/\lambda f)}{\pi D r/\lambda f}\right],$$

which is shown in Figure 3. The beamwidth (full width at half maximum) for this diffraction-limited system is approximately $\lambda f/D$.

Image Reconstruction from Noiseless Data

When an optical system is subject to aberrations in the plane of the aperture, evidence of the effect is displayed as a narrowing of the optical transfer function

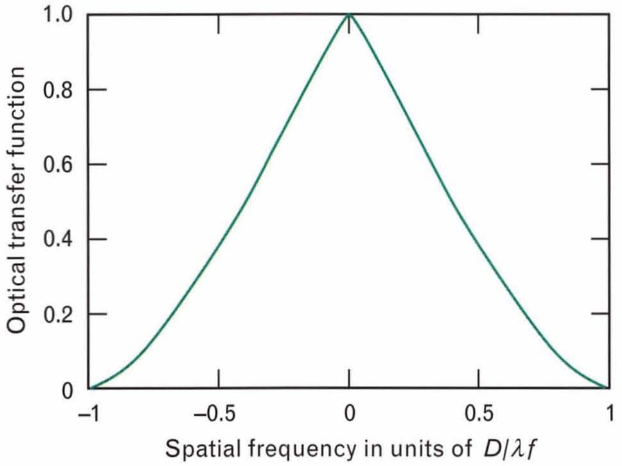

FIGURE 2. Optical transfer function for a circular aperture of diameter D. This function is approximately triangular in shape and has a cutoff frequency of $D/\lambda f$.

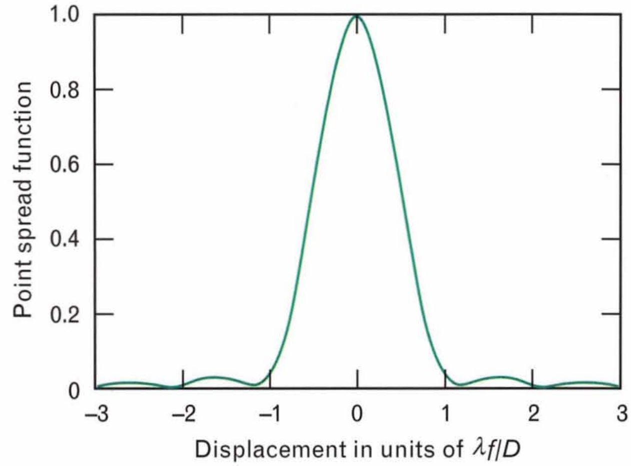

FIGURE 3. Point spread function for a circular aperture of diameter D. This plot represents the diffraction-limited impulse response of a perfect collector.

(due to the attenuation of high-spatial-frequency image components) and a broadening of the point spread function. As suggested by Equation 3, the diffraction-limited image can be recovered from the intensity data if the optical transfer function of the aperture-plane distortion has been measured; i.e.,

$$\mathcal{F}\{I\} = \left\langle \frac{\mathcal{F}\{I'\}}{OTF_d} \right\rangle = OTF_c \left\langle \frac{\mathcal{F}\{I'\}}{OTF} \right\rangle ,$$

where the nonsubscripted OTF represents the total optical transfer function of the receiver, as computed in Equation 4. The indicated ensemble average is appropriate when multiple images of a dim object are collected, each of which may be associated with a different distortion pattern. The net effect of this operation is to apply gain at spatial frequencies for which the total receiver OTF is less than the optical transfer function for a circular aperture. The diffraction-limited image is recovered from the inverse transform of this expression; for computational convenience the operand has been modified to avoid division by a complex number:

$$I = \mathcal{F}^{-1}\left\{ OTF_c \left\langle \frac{OTF^* \mathcal{F}(I')}{|OTF|^2} \right\rangle \right\}.$$

This relationship assumes, however, that the corrupted image I' is noiseless and that the composite optical transfer function is non-zero within the transmission band of the diffraction-limited transfer function. Because neither of these requirements is likely to be satisfied with real data, a technique must be found to remove singularities and limit the amount of gain applied in spectral regions where the signal-to-noise ratio is low. Naive attempts to implement Fourier deconvolution usually fail when these problems are not properly addressed.

Optimal Reconstruction of Images with Finite Noise

The general problem of image reconstruction can be treated as one of optimal estimation in which we wish to reproduce a given signal as accurately as possible in the presence of additive noise. The signal in this case is the diffraction-limited image $I = O \otimes PSF_c$. The recorded signal is the sum of the corrupted image I' and a noise component n. The data-recovery process is assumed to involve a convolution with the two-dimensional operator g, which is optimized to obtain the best picture quality,

$$\begin{aligned} \tilde{I} &= g \otimes (O \otimes PSF_c \otimes PFS_d + n) \\ &= g \otimes (I' + n). \end{aligned} \tag{5}$$

This relationship is a variant of a standard optimization problem for additive noise that was first solved by Norbert Wiener [8]. Similar problems have been treated previously in the literature [3, 9, 10], and the standard result is

$$\mathcal{F}\{g\} = \frac{\mathcal{F}\{I\}\mathcal{F}^*\{I'\}}{\left|\mathcal{F}\{I'+n\}\right|^2} = \frac{\mathcal{F}\{I\}\mathcal{F}^*\{I'\}}{\left|\mathcal{F}\{I'\}\right|^2 + \left|\mathcal{F}\{n\}\right|^2}. \tag{6}$$

Equation 6 describes the operator whose output will most nearly match the noise-free image formed by a diffraction-limited aperture. Combining this expression with the Fourier transform of the recovered image as defined in Equation 5 provides a complete description of the desired transformation,

$$\tilde{I} = \mathcal{F}^{-1}\left\{ OTF_c \left\langle \frac{OTF^*\mathcal{F}\{I'+n\}}{\left|OTF\right|^2 + F_n/F_o} \right\rangle \right\}, \tag{7}$$

where $F_o = \left|\mathcal{F}\{O\}\right|^2$ and $F_n = \left|\mathcal{F}\{n\}\right|^2$ are the power spectral density functions associated with the object and the system noise, respectively. This operation is known as *Wiener deconvolution.*

The successful application of Wiener deconvolution is strongly dependent on our ability to estimate the ratio of the noise and object power spectra, F_n/F_o. For small sources, such as an isolated star, this quantity is a constant equal to the square of the signal-to-noise ratio of the total optical power.

Wiener Deconvolution Applied to Terrain Imagery

In this section we discuss the form of Wiener deconvolution for terrestrial scenes. The explicit inclusion of the object power spectrum F_o in the deconvolution process described by Equation 7 provides a strong motivation to develop an analytical representation of this quantity that has general applicability. For optical and infrared imagery of terrain features, a first-order Markov description of the autocorrelation function is frequently employed for this purpose [11]. The Markov description is

$$\Re_0(\rho) = \sigma_o^2 e^{-\left|\rho/\rho_o\right|},$$

where σ_o^2 is the intensity variance of the scene, and the characteristic correlation length ρ_o is defined as

$$\rho_o \equiv \frac{1}{\sigma_o^2}\int_0^\infty \Re_0(\rho)\,d\rho. \tag{8}$$

This description is a special case of a more general formalism [12],

$$\begin{aligned}\Re_0(\rho) = {} & \frac{2\sigma_o^2}{\Gamma(\nu)}\left(\frac{\sqrt{\pi}\,\Gamma(\nu+1/2)\rho}{2\Gamma(\nu)\rho_o}\right)^\nu \\ & \times K_\nu\left(\frac{\sqrt{\pi}\,\Gamma(\nu+1/2)\rho}{\Gamma(\nu)\rho_o}\right).\end{aligned} \tag{9}$$

Equation 9 reproduces the Markov expression when $\nu = 1/2$. If the spatial statistics of the scene are radially symmetric, the two-dimensional power spectral density function is obtained directly from the Hankel transform of $\Re_0$,

$$\begin{aligned}F_o(f_r) = {} & \frac{4\Gamma(\nu)\Gamma(\nu+1)\sigma_o^2\rho_o^2}{\left[\Gamma(\nu+1/2)\right]^2} \\ & \times\left[1 + \left(\frac{2\sqrt{\pi}\,\Gamma(\nu)\rho_o f_r}{\Gamma(\nu+1/2)}\right)^2\right]^{-(1+\nu)}.\end{aligned} \tag{10}$$

This function displays an $f_r^{-2(1+\nu)}$ characteristic at high frequencies.

The sensor noise is assumed to be white, which implies that the noise spectrum is constant to first order. For a discrete data-collection system the signal will be constant over a square pixel of dimension ρ_{pix}. When the noise is spatially uncorrelated from pixel to pixel, this model results in a triangular-shaped autocorrelation function having a value of σ_n^2 at the origin; the associated power spectral density function of the noise in rectangular coordinates is

$$\begin{aligned}&F_n(f_x, f_y) = \\ &\quad \sigma_n^2\rho_{\text{pix}}^2\left[\frac{\sin^2(\pi\rho_{\text{pix}}f_x)}{(\pi\rho_{\text{pix}}f_x)^2}\right]\left[\frac{\sin^2(\pi\rho_{\text{pix}}f_y)}{(\pi\rho_{\text{pix}}f_y)^2}\right].\end{aligned}$$

In the limit that the characteristic correlation length of the scene is much larger than the dimensions of a sample element (i.e., $\rho_o >> \rho_{\text{pix}}$) we can assume that $F_n(f_r) \approx F_n(0)$. When this result is combined with the power spectral density function given in Equation 10, the frequency-dependent signal-to-noise ratio is found to be

FIGURE 4. Landsat imagery of the greater Boston area. This color rendition represents a combination of separate red, green, and blue images obtained by the satellite's Thematic Mapper. The spatial resolution of this picture as created by the Landsat imaging system is 29 m. A corrupted version of this image was used to illustrate the image-restoration performance of the Fourier deconvolution process.

$$\frac{F_o(f_r)}{F_n(f_r)} \approx \left(\frac{\sigma_o^2}{\sigma_n^2}\right)\left(\frac{\rho_o^2}{\rho_{\text{pix}}^2}\right)\frac{4\Gamma(\nu)\Gamma(\nu+1)}{\left[\Gamma(\nu+1/2)\right]^2} \times\left[1+\left(\frac{2\sqrt{\pi}\,\Gamma(\nu)\rho_o f_r}{\Gamma(\nu+1/2)}\right)^2\right]^{-(1+\nu)} . \tag{11}$$

Later in this article, we use the Landsat terrain image of the Boston area shown in Figure 4 to illustrate the performance of the deconvolution process; therefore, it is useful at this point to investigate the statistical properties of these data. Figure 4 shows a 1024×1024 visible image covering a 30-km^2 region of eastern Massachusetts. Figure 5 gives the average radial autocorrelation function for this scene. By using Equation 8 we compute a characteristic correlation length of approximately 1 km from these data, and we obtain a best fit to the correlation model specified in Equation 10 for $\nu = 0.07$. Both of these numbers

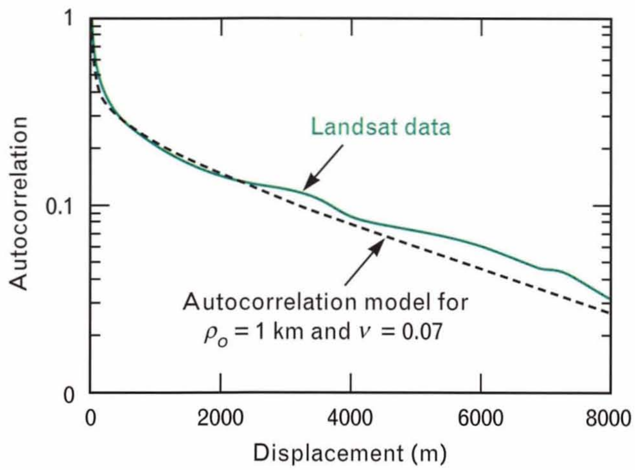

FIGURE 5. Autocorrelation function of the Landsat imagery within the 630-to-690-nm waveband. A correlation length of 1 km is derived for these data on the basis of a parametric curve fit to the autocorrelation model given in Equation 9. A quantitative estimate of the correlation length is essential to the Wiener deconvolution process.

are consistent with parameters obtained in prior analyses of infrared terrain imagery [13].

If we make the assumption that ν is typically less than 0.5 for the scenes of interest and ρ_o is likely to be much larger than the diffraction-limited resolution of the sensor, then Equations 7 and 11 can be combined in the following manner to form the Wiener estimate of the diffraction-limited image,

$$\tilde{I} = \mathcal{F}^{-1}\left\{ OTF_c \left[\frac{OTF^* \mathcal{F}(I' + n)}{\left|OTF\right|^2 + C_\nu f_r^{2+2\nu}} \right] \right\}, \quad (12)$$

where

$$C_\nu = 4^\nu \pi^{1+\nu} \nu^{-(1+2\nu)} \rho_{\text{pix}}^2 \rho_o^{2\nu} \left(\frac{\sigma_n}{\sigma_o} \right)^2 . \quad (13)$$

We now discuss the application of this algorithm to a specific image-reconstruction problem.

Restoration of Image Data Collected by Sparse-Aperture Reconnaissance Satellites

One application of Wiener deconvolution that is potentially of great interest to both the defense community and the civil sector is the restoration of optical imagery collected by sparse-aperture receivers. Size and weight parameters are primary considerations in the design of high-resolution surveillance satellites, and the use of aperture-thinning techniques could result in a significant reduction of the costs associated with payload deployment. Consider, for example, the three-petal shape shown in Figure 6, which has a collection area only one-tenth that of the filled aperture. Such a structure could be folded into a compact package deployable by a relatively small and inexpensive launch vehicle, as suggested in Figure 7. Although this particular design is not optimal for high-quality image recovery—indeed, the distributed-collector geometries proposed by Golay [14] are much better suited for this purpose (see the sidebar entitled "Golay Receiver Configurations")—it has the benefit of simplicity and it also provides a rather stressing test of the deconvolution process.

The possibility of reducing the payload weight of a reconnaissance satellite by an order of magnitude is clearly intriguing. However, as a first step in proving that the aperture-thinning concept is economically viable, we must demonstrate that the image quality achievable with a sparse-aperture receiver is compa-

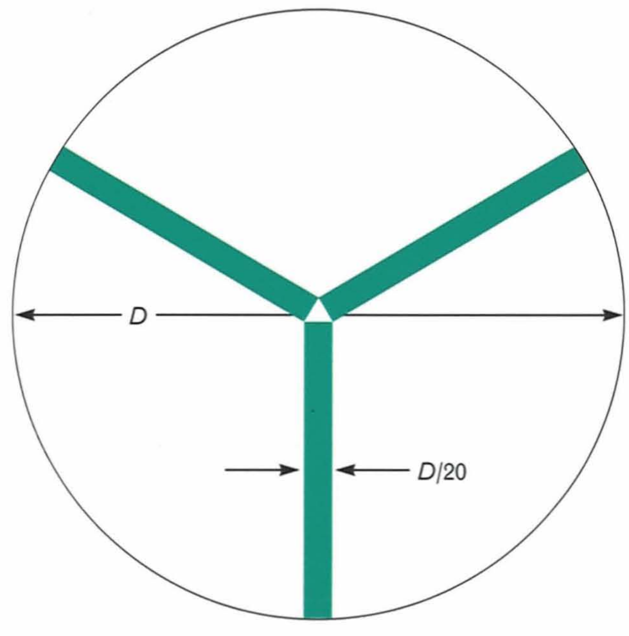

FIGURE 6. Illustration of a three-segment sparse aperture having an outer diameter of D and segments of width $D/20$. The collection area of the design shown in this figure is approximately 10% of the full aperture.

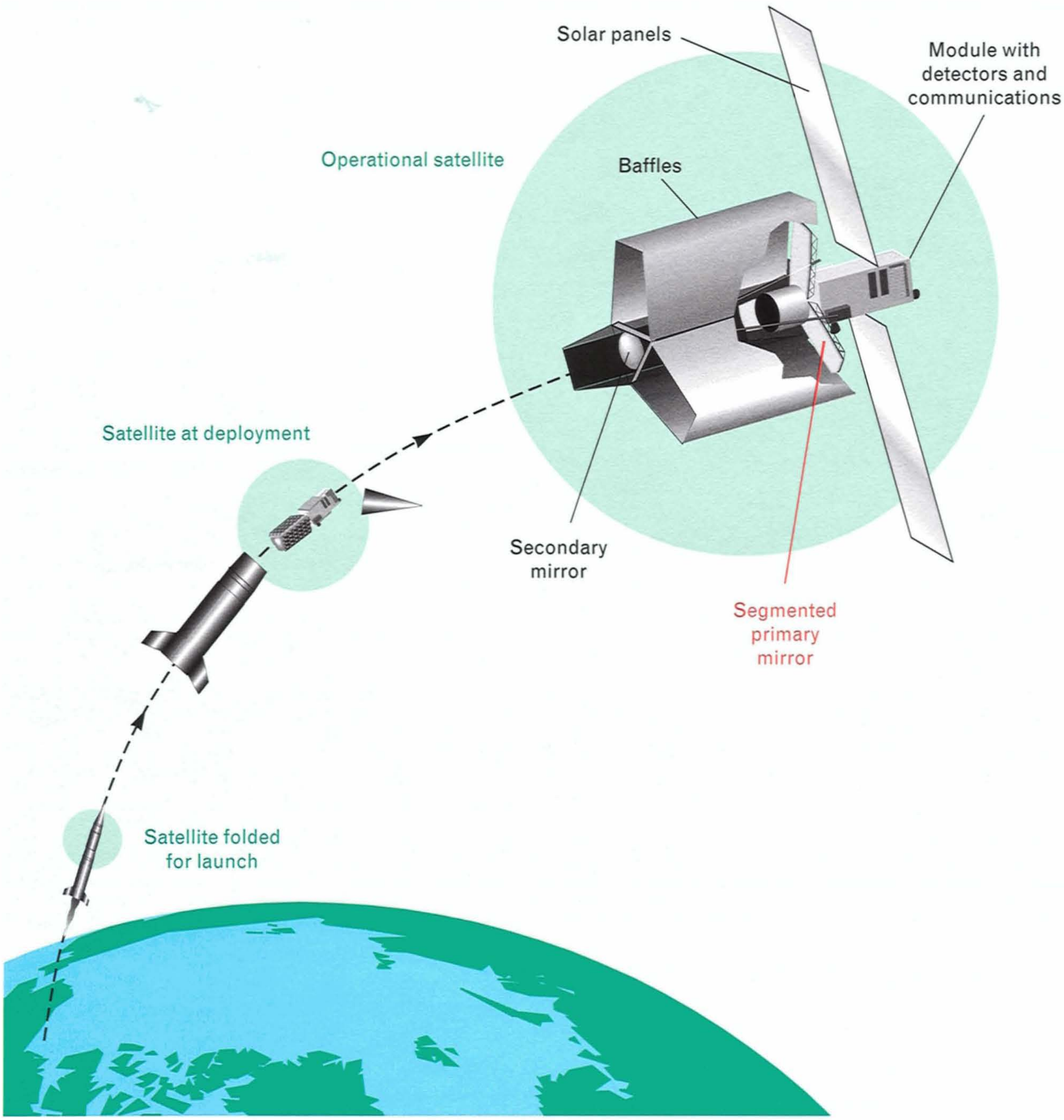

FIGURE 7. A sparse-aperture reconnaissance system could be placed into orbit by a small and relatively inexpensive launch vehicle. Upon deployment the aperture sections would be unfolded and phased to form a coherent receiver.

rable to that obtained with a conventional receiver. In the next section we address the issue of performance by using quantitative comparisons involving the modulation transfer function, point spread function, and processing simulations incorporating down-looking satellite imagery.

Comparative Analysis of Receiver Modulation Transfer Function and Point Spread Functions

The modulus of the optical transfer function, or modulation transfer function *MTF*, associated with the three-petal structure illustrated in Figure 6 dis-

GOLAY RECEIVER CONFIGURATIONS

THE THREE-PETAL RECEIVER investigated in this article was selected to demonstrate the application of image-reconstruction algorithms to a lightweight receiver structure that could be compactly folded into a relatively small and inexpensive launch vehicle. The three-petal geometry does not, however, provide the optimal image quality for low-fill-factor collectors.

Sparse-aperture optical receivers have been studied for at least two decades; some of the first work in this field was performed in the early 1970s by Marcel Golay [1]. Golay developed a technique for positioning small independent elements to form arrays having nonredundant autocorrelation functions. Receiver designs of this type produce optical transfer functions that uniformly fill the frequency space within the diffraction-limited transmission band of a filled aperture of comparable dimensions.

Figure A illustrates an example of a nine-element Golay system having a 10% fill factor within a circular region. The array components are positioned so that no more than two of the elements overlap for autocorrelation function displacements larger than one element diameter. This structure results in a modulation transfer function that provides a dense sampling of the spatial frequencies transmitted by the full aperture, as shown in Figure B. In general, a Golay structure containing n independent elements will generate a modulation transfer function exhibiting $n^2 - n + 1$ separate regions. The raw imagery generated by such apertures is particularly well suited for reconstruction by methods of post-processing data enhancement.

References

1. M.J.E. Golay, "Point Arrays Having Compact, Nonredundant Autocorrelations," *J. Opt. Soc. Am.* **61**, 272 (1971).

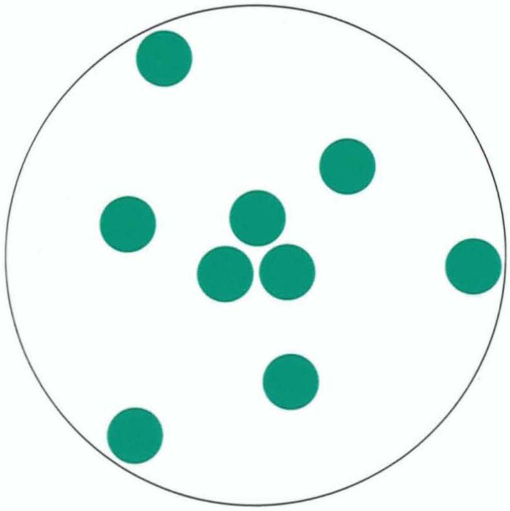

FIGURE A. Example of a Golay structure incorporating nine receiver elements, creating a 10% fill factor within a circular region. Golay systems position elements to form arrays having nonredundant autocorrelation functions, and they can be constructed by using an arbitrary number of array components.

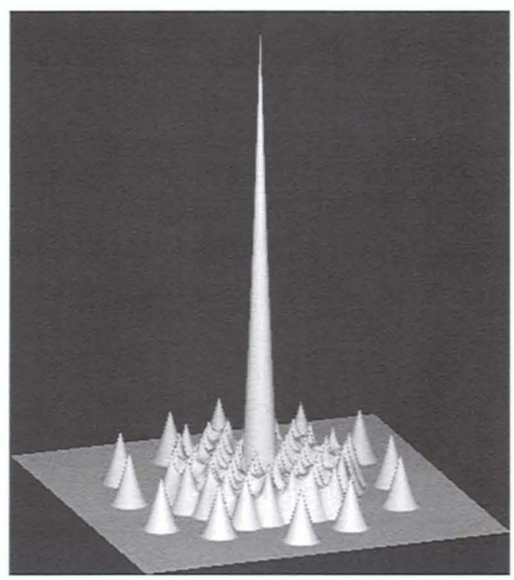

FIGURE B. The optical transfer function associated with the nine-element Golay system. The central core results from the overlap of all array components near the origin of the autocorrelation function, whereas each of the remaining seventy-two peaks arises from the overlap of exactly two elements.

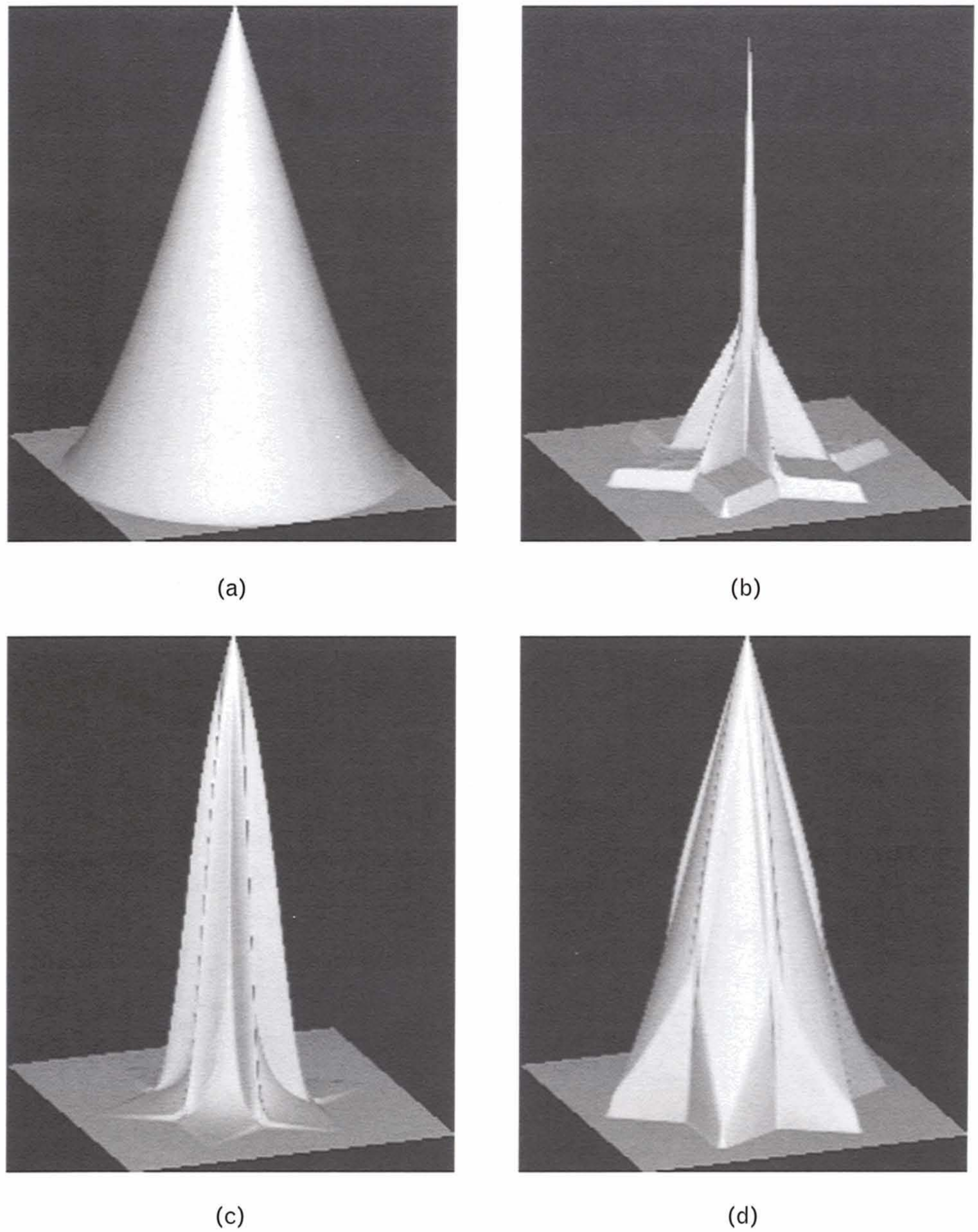

FIGURE 8. Comparison of system modulation transfer functions for (a) a diffraction-limited circular aperture, (b) a three-petal receiver having a 10% fill factor, (c) Wiener deconvolution for $\sigma_o/\sigma_n = 10$, and (d) Wiener deconvolution for $\sigma_o/\sigma_n = 100$. This progression demonstrates the ability of Fourier deconvolution to transform, under favorable signal-to-noise conditions, the highly aberrated modulation transfer function of a sparse-aperture receiver into a transfer function that is nearly identical to the modulation transfer function of a filled circular aperture.

plays a six-fold symmetry in which the high spatial frequencies are heavily attenuated in comparison with the modulation transfer function of a circular aperture, as shown in Figures 8(a) and 8(b). Notice, however, that most of the region within the band limit of the circular aperture in Figure 8(a) is non-zero, which is a first indication that deconvolution techniques are likely to provide significant improvement under favorable signal-to-noise conditions. The effective modulation transfer function of the Wiener decon-

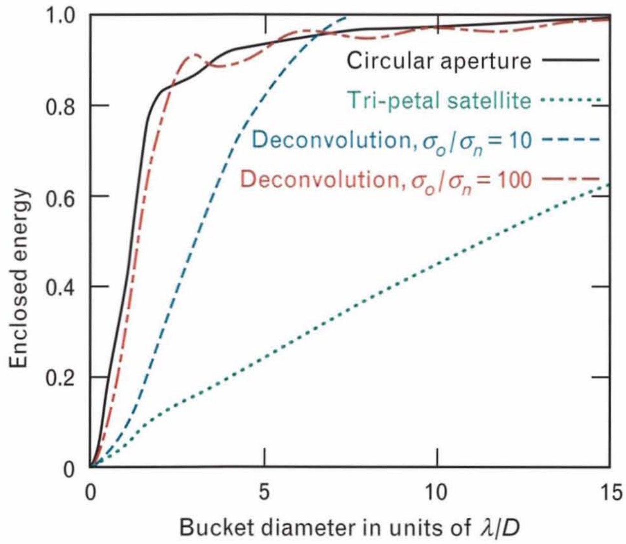

FIGURE 9. Comparison of cumulative point spread functions. The enclosed-energy profile provides a convenient means of relating the ability of an imaging system to concentrate light to the focusing capability of a diffraction-limited receiver. (Note that the curves for deconvolution are not monotonic because the point spread functions associated with these operations include negative values.) This figure demonstrates that sparse-aperture imagery having a signal-to-noise ratio of 100 can be processed to produce pictures nearly as sharp as those generated by a filled circular aperture.

volution process is the Fourier-space multiplicative factor appearing in Equation 12,

$$MTF_{\text{Wiener}} \approx \left| \frac{OTF_c\, OTF^2}{\left|OTF\right|^2 + C_v f_r^{2+2v}} \right|,$$

where C_v is defined in Equation 13. We can evaluate this function by applying the terrain parameters derived in Figure 5; namely, $\rho_{\text{pix}} = 29$ m, $\rho_o = 1$ km, and $v = 0.07$. The results of this exercise for signal-to-noise levels equivalent to $\sigma_o/\sigma_n = 10$ and $\sigma_o/\sigma_n = 100$ are shown in Figures 8(c) and 8(d), respectively. In the image reconstruction example shown in Figure 8(c) the Wiener deconvolution process actually reduces the modulation transfer function at the highest spatial frequencies, which results in a slight broadening of the point spread function. In the image reconstruction example shown in Figure 8(d), essentially all of the non-zero spatial frequencies have been restored to levels comparable to those of the diffraction-limited circular-aperture system.

The overall improvement in the point spread function due to the application of Wiener deconvolution is reflected in the enclosed-energy plots shown in Figure 9. Each of the four curves shown in this illustration represents the encircled point-spread-function energy as a function of bucket diameter, which provides a rough estimate of the effective system resolution. If the diameter at which the 50% value is achieved is selected as the resolution criterion, the resolution of the three-petal satellite would be judged to be a factor of nine worse than the resolution for the circular aperture. By contrast, image deconvolution for $\sigma_o/\sigma_n = 10$ yields a degradation factor of only three, and the $\sigma_o/\sigma_n = 100$ case is nearly identical to the performance of a filled circular aperture.

Application of Wiener Deconvolution to Landsat Data

To test the utility of a sparse-aperture structure used in conjunction with an appropriate data processor, we selected a 256 × 256 section of the Landsat image shown in Figure 4 for study. To assess the capability of the processing technique fairly, we first convolved these data with a circular-aperture point spread function having a profile comparable to the dimensions of a single pixel. Specifically, the relationships between the diameter, focal length, and optical wavelength of the satellite's aperture are related to the pixel dimensions within the plane of the sensor in the following manner:

$$\frac{\lambda f}{D} = \rho_{\text{pix}} .$$

This expression also establishes the Fourier-transform scaling between the aperture and image planes. The resulting picture, shown in Figure 10(a), provides a high-resolution baseline against which the reconstructed images can be compared.

To first order, the smearing introduced by the three-petal collector is the ratio of the full-aperture diameter to the petal width; this ratio is approximately twenty for the test example used in this study. The severity of the associated image degradation is clearly evident in Figure 10(b), which is the result of convolving the Landsat data with the three-petal

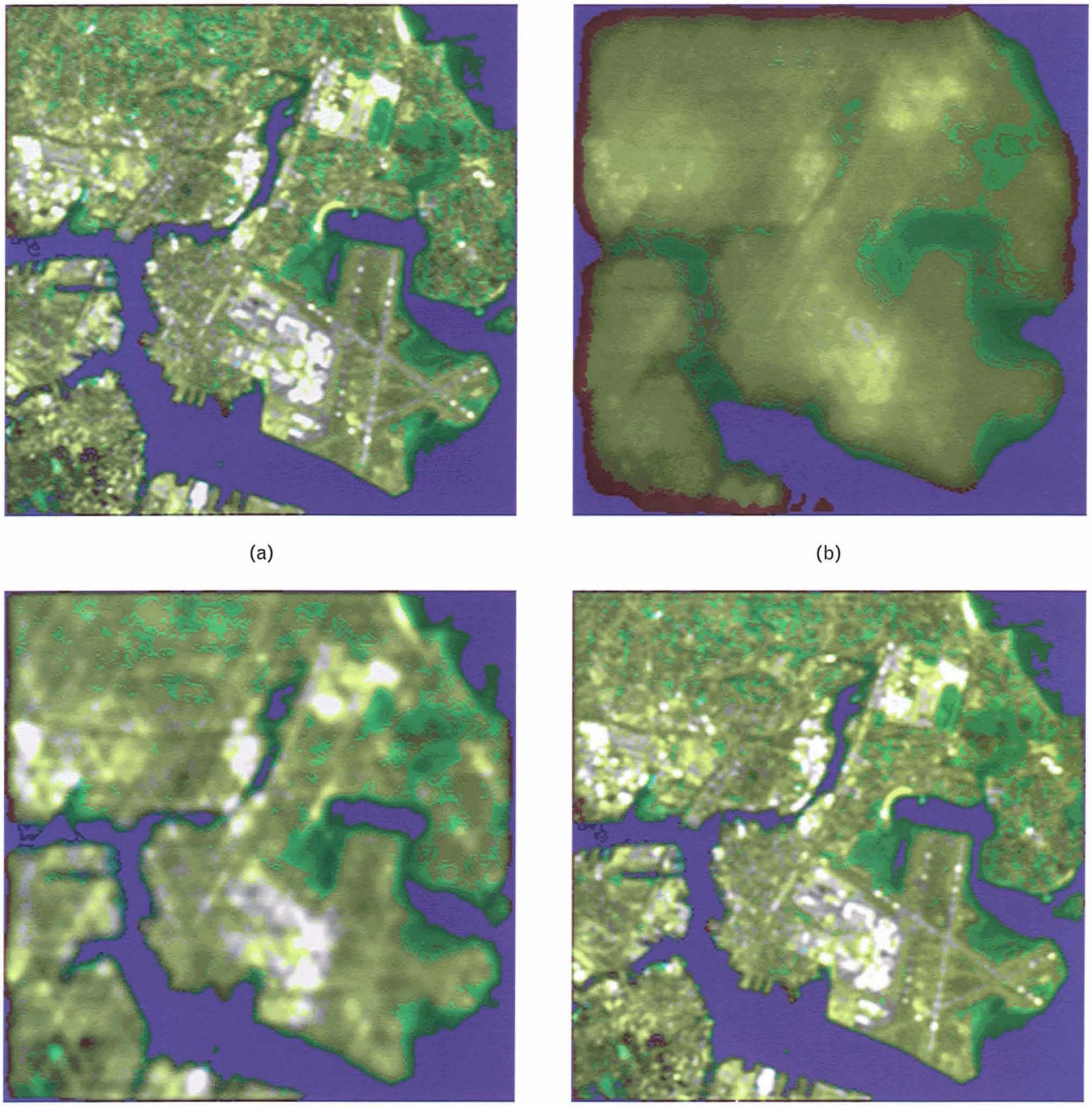

(a) (b) (c) (d)

FIGURE 10. Comparison of images obtained from (a) a diffraction-limited circular aperture, (b) a three-petal receiver having a 10% fill factor, (c) Wiener deconvolution for $\sigma_o/\sigma_n = 10$, and (d) Wiener deconvolution for $\sigma_o/\sigma_n = 100$. This qualitative comparison offers convincing evidence that Fourier-space restoration techniques can effectively correct optical distortion introduced by sparse-aperture receivers.

receiver's point spread function. Because of the strong attenuation of the high-spatial-frequency components of the original picture, only the grossest details of this image are discernible. We must keep in mind, however, that most of these components have not been eliminated, but only reduced in amplitude.

Wiener restoration of the suppressed spatial frequencies is demonstrated in Figures 10(c) and 10(d), which represent optimal reconstructions for $\sigma_o / \sigma_n =$ 10 and $\sigma_o / \sigma_n =$ 100, respectively. The first of these two images displays a significant enhancement in resolution compared with that for the three-petal collector in Figure 10(b), whereas the second is nearly as sharp as the picture derived from the convolution of the raw data with the point spread function for a circular aperture. Although these tests are admittedly qualitative, they provide convincing evidence of the feasibility and potential benefits of the reconstruction concept.

From a cost/performance standpoint, there is an obvious advantage in replacing massive collectors with lightweight telescopes that are coupled to sophisticated data processors, particularly for space-based applications. For the highly thinned design chosen for this investigation, a signal level on the order of a hundred to a thousand times larger than that required for conventional imaging would be needed to overcome collection losses and satisfy the Wiener restoration criteria. However, as indicated in the appendix, "Signal-to-Noise Calculations for a Representative Reconnaissance Scenario," it is not unreasonable to expect that these criteria would be met for a low-earth-orbit satellite. Furthermore, a more detailed system trade-off analysis might uncover collector configurations and image processing approaches that would reduce this requirement significantly.

Conclusions

This article offers convincing evidence of the utility of Fourier deconvolution in extracting improved imagery from non-ideal optical receivers. Although the quality of the recovered image data is ultimately limited by the cutoff frequency of the system's optical transfer function, highly attenuated frequency components can be recovered as long as the signal-to-noise ratio exceeds the gain required for restoration. These conditions are met for many scenarios of practical interest.

To demonstrate the potential utility of image reconstruction, we applied the optical transfer function for a highly thinned optical collector to Landsat imagery, and the reconstructed pictures were compared with images obtained with a conventional telescope. Under favorable signal conditions the reconstructed images from the sparse-aperture collector nearly match those obtained by a filled circular aperture. This result lends strong support to the feasibility of constructing inexpensive, lightweight surveillance satellites employing folded-mirror architectures.

Acknowledgments

The Landsat images shown in this article were provided by John Kerekes, to whom we are indebted for both the pictures and the supporting information. We would also like to thank Susanne LePage, who was involved in the initial design of the image reconstruction codes used in this investigation.

REFERENCES

1. R. Nathan, "Digital Video Handling," Jet Propulsion Laboratory Technical Report, 32-877 (5 Jan. 1966).
2. J.L. Harris, Sr., "Image Evaluation and Restoration," *J. Opt. Soc. Am.* **56**, 569 (1966).
3. C.W. Helstrom, "Image Restoration by the Method of Least Squares," *J. Opt. Soc. Am.* **57**, 297 (1967).
4. D. Slepian, "Linear Least-Squares Filtering of Distorted Images," *J. Opt. Soc. Am.* **57**, 918 (1967).
5. W.K. Pratt, "Generalized Wiener Filter Computation Techniques," *IEEE Trans. Computers* **21**, 636 (1972).
6. A. Labeyrie, "Attainment of Diffraction Limited Resolution in Large Telescopes by Fourier Analyzing Speckle Patterns in Star Images," *Astron. Astrophys.* **6**, 85 (1970).
7. J.W. Goodman, *Statistical Optics*, John Wiley, New York (1985).
8. N. Wiener, *Extrapolation, Interpolation, and Smoothing of Stationary Time Series,* John Wiley, New York (1949).
9. K.R. Castleman, *Digital Image Processing,* Prentice-Hall, Englewood Cliffs, NJ (1979).
10. R.C. Brown, *Introduction to Random Signal Analysis and Kalman Filtering,* John Wiley, New York (1983).
11. W.K. Pratt, *Digital Image Processing,* John Wiley, New York (1978).
12. W.I. Futterman, E.L. Schweitzer, and J.E. Newt, "Estimation of Scene Correlation Lengths," *SPIE* **1486**, 127 (1991).
13. G.J. Zissis, ed., *The Infrared & Electro-Optical Systems Handbook, Vol. 1,* SPIE Optical Engineering Press, Bellingham, WA (1993).
14. M.J.E. Golay, "Point Arrays Having Compact, Nonredundant Autocorrelations," *J. Opt. Soc. Am.* **61**, 272 (1971).

APPENDIX: SIGNAL-TO-NOISE CALCULATIONS FOR A REPRESENTATIVE RECONNAISSANCE SCENARIO

SPARSE-APERTURE OPTICAL SYSTEMS are inherently less efficient at collecting photons than filled apertures of comparable dimension. The effects of these losses can be further exacerbated by the noise amplification associated with the implementation of an optical-transfer-function enhancement process. To establish overall concept viability, we must demonstrate that the requisite signal-to-noise ratio can be achieved in a real reconnaissance scenario.

For an unresolved-target viewing geometry, illustrated in Figure 1, a square detector of dimension d collects light originating from a ground patch of area $(\rho_{\text{pix}})^2 = (Rd/f)^2$, where f is the telescope focal length and R is the altitude of the reconnaissance satellite. The collection aperture subtends a solid angle equal to $(\pi/4)(D/R)^2$ with respect to the ground, where D is the aperture diameter. This geometry results in the following expression for the number of electrons generated by the sensor within the spectral bandwidth $\lambda_1 < \lambda < \lambda_2$:

$$N_e = \frac{\pi d^2}{4(f/\text{no})^2} \int_{\lambda_1}^{\lambda_2} \left(\frac{\lambda}{hc}\right) \underbrace{\alpha \beta \tau_d \eta(\lambda)}_{\substack{\text{collection}\\\text{efficiency}}} \; \underbrace{\varepsilon(\lambda) N(\lambda)}_{\substack{\text{source}\\\text{spectral radiance}}} \, d\lambda \,, \tag{1}$$

where d is the detector size, f/no is the camera f number, α is the net system transmission, β is the telescope thinning factor, τ_d is the sensor dwell time, $\eta(\lambda)$ is the detector quantum efficiency, $N(\lambda)$ is the spectral radiance, and $\varepsilon(\lambda)$ is the source reflectivity (for reflected solar radiation) or emissivity (for blackbody radiation).

To satisfy the Nyquist criterion the detector size should be approximately equal to $\lambda f / 2D$, in which case Equation 1 can be rewritten as

$$N_e = \frac{\pi \alpha \beta \tau_d \lambda_c^2}{16} \int_{\lambda_1}^{\lambda_2} \left(\frac{\lambda}{hc}\right) \eta(\lambda) \varepsilon(\lambda) N(\lambda) \, d\lambda \,, \tag{2}$$

where λ_c is the center of the spectral bandwidth. For some missions it may be advantageous to degrade the sensor's resolution intentionally in order to increase the total field of view or reduce the data bandwidth. As a result, the dimensions of the pixel ground patch would establish the size of the detector, so that $d = f\rho_{\text{pix}}/R$ and the following form is obtained:

$$N_e = \frac{\pi \alpha \beta \tau_d \rho_{\text{pix}}^2 D^2}{4R^2} \int_{\lambda_1}^{\lambda_2} \left(\frac{\lambda}{hc}\right) \eta(\lambda) \varepsilon(\lambda) N(\lambda) \, d\lambda \,. \tag{3}$$

Equation 2 is appropriate for high-altitude infrared systems, whereas Equation 3 is applicable for most low-altitude missions.

The dwell time of the system is directly related to the satellite's orbital period T_o. For a circular orbit,

$$T_o = 2\pi \sqrt{\frac{(R + R_e)^3}{GM_e}} \,,$$

where $G = 6.67 \times 10^{-11}$ nt-m^2/kg^2 is the gravitational constant, $M_e = 5.98 \times 10^{24}$ kg is the mass of the earth,

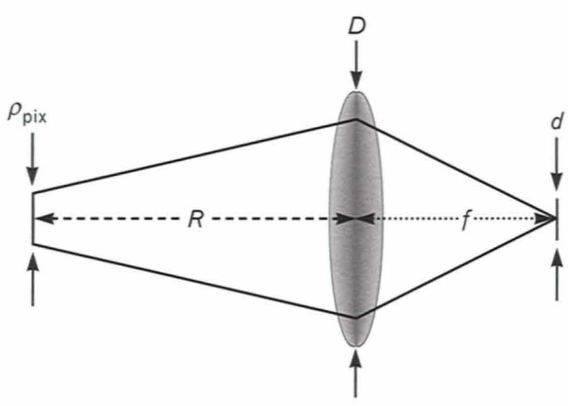

FIGURE 1. Light-collection geometry for a telescope having a collection aperture with diameter D and focal length f. The square detector with dimension d collects light from a ground patch with dimension ρ_{pix} at a reconnaissance altitude R.

$R_e = 6.36 \times 10^6$ m is the radius of the earth, and R is the satellite's altitude. If the motion of the satellite is used to generate two-dimensional images in a "push broom" fashion, the pixels on the ground are scanned at a velocity of $v = 2\pi R_e / T_o$. For this particular scan configuration, the sensor's dwell time τ_d and the ground resolution ρ_{pix} are constrained in the following manner:

$$\tau_d = n_d \frac{\rho_{\text{pix}}}{v} = \frac{n_d \rho_{\text{pix}} T_o}{2\pi R_e},$$

where the parameter n_d represents the number of pixels in the detector array along the direction of motion that are used for time delay and integration. For low-altitude satellites the orbital period is almost independent of the satellite altitude, in which case the dwell time is proportional to R/D.

At this point we must introduce appropriate expressions for the spectral radiance. For blackbody radiation the radiance N as a function of wavelength is given by

$$N(\lambda) = \frac{2hc^2}{\lambda^5 \left[\exp\left(\dfrac{hc}{\lambda k T} \right) - 1 \right]}, \tag{4}$$

where $c = 3.00 \times 10^8$ m/sec is the velocity of light, $h = 6.63 \times 10^{-34}$ W-sec^2 is Planck's constant, $k = 1.38 \times 10^{-23}$ W-sec/K is Boltzmann's constant, and $T \approx 300$ K is the source temperature [1]. For most scenes the image contrast is determined primarily by temperature fluctuations in the local terrain. To a good approximation, the signal can be characterized as the product of the scene standard deviation σ_T and the derivative of Equation 2 with respect to temperature:

$$\text{signal} = \frac{\partial N_e}{\partial T} \sigma_T = \frac{\pi \alpha \beta \tau_d \lambda_c^2 \sigma_T}{16} \times \int_{\lambda_1}^{\lambda_2} \left(\frac{\lambda}{hc} \right) \eta(\lambda) \varepsilon(\lambda) \left\{ \frac{2h^2 c^3 \exp\left(\dfrac{hc}{\lambda k T} \right)}{k T^2 \lambda^6 \left[\exp\left(\dfrac{hc}{\lambda k T} \right) - 1 \right]^2} \right\} d\lambda .$$

Typically, the scene standard deviation σ_T is in the range of 1 to 5°C [2].

The noise generated by the sensor includes several terms, the most important of which are quantum noise n_Q due to photon-arrival statistics, additive temporal noise n_{AT} primarily due to readout-amplifier fluctuations, and multiplicative fixed-pattern noise n_{MFP} [3]. The magnitude of the first and third of these effects is dependent on the average number of collected electrons $\overline{N}_e$, where

$$n_Q = \sqrt{\overline{N}_e}$$

and

$$n_{MFP} = U_c \overline{N}_e ,$$

and where U_c is the array uniformity following a two-point response correction. The total noise (standard deviation of the temporal and spatial fluctuations) is the square root of the sum of the variances, or

$$\begin{aligned} \text{noise} &= \sqrt{n_Q^2 + n_{AT}^2 + n_{MFP}^2} \\ &= \sqrt{\overline{N}_e + n_{AT}^2 + U_c^2 \overline{N}_e^2} . \end{aligned} \tag{5}$$

For a diffraction-limited infrared system sampled at the Nyquist frequency, the average number of electrons collected by a pixel during a dwell time τ_d is

$$\overline{N}_e = \frac{\pi \alpha \beta \tau_d \lambda_c^2}{16} \times \int_{\lambda_1}^{\lambda_2} \left(\frac{\lambda}{hc} \right) \eta(\lambda) \varepsilon(\lambda) \left\{ \frac{2hc^2}{\lambda^5 \left[\exp\left(\dfrac{hc}{\lambda k T} \right) - 1 \right]} \right\} d\lambda .$$

The noise for this system is determined by substituting this equation into Equation 5. Nominal values for η, n_{AT}, and U_c for large InSb detector arrays are 0.5, 250 rms electrons, and 1%, respectively.

For reflected solar radiation the expression is more complex because a number of additional parameters are involved, such as the angle between the sun and the normal to the earth's surface. To first order, the reflected radiation can be modeled as a 5900 K blackbody with an emissivity that incorporates all of the geometrical factors involved in the reflection of light from the sun to the satellite. By comparing data given in *The Infrared Handbook* [4] with the output of a blackbody having unit emissivity, we can develop the following approximation from Equations 3 and 4:

$$\overline{N}_e = \frac{(3\times 10^{-6})\pi\alpha\beta\tau_d\rho_{\text{pix}}^2 D^2}{4R^2} \times \int_{\lambda_1}^{\lambda_2}\left(\frac{\lambda}{hc}\right)\eta(\lambda)\left\{\frac{2hc^2}{\lambda^5\left[\exp\left(\frac{hc}{\lambda kT}\right)-1\right]}\right\}d\lambda\,, \tag{6}$$

where $T = 5900$ K. In this case the contrast is due to fractional changes in the terrain reflectivity σ_r, which is perhaps on the order of 0.1. Thus the signal is expected to be

$$\text{signal} = \frac{(3\times 10^{-6})\pi\alpha\beta\tau_d\rho_{\text{pix}}^2 D^2\sigma_r}{4R^2} \times \int_{\lambda_1}^{\lambda_2}\left(\frac{\lambda}{hc}\right)\eta(\lambda)\left\{\frac{2hc^2}{\lambda^5\left[\exp\left(\frac{hc}{\lambda kT}\right)-1\right]}\right\}d\lambda\,.$$

The noise for this system is obtained by substituting Equation 6 into Equation 5; nominal values for η, n_{AT}, and U_c for large Si detector arrays are 0.8, 5 rms electrons, and 0.25%, respectively.

Table 1 establishes a baseline sensor construct involving a platform orbiting at an altitude of a thou-

Table 1. Parameter List For Baseline Signal-to-Noise Calculation

Parameter	*Symbol*	*Visible sensor*	*IR sensor*
Detector material		Si	InSb
Center wavelength	λ_c	0.6 μm	4 μm
Satellite altitude	R	1000 km	1000 km
Aperture diameter	D	10 m	10 m
Detector array size	n_d	1024×1024	1024×1024
System transmission	α	0.5	0.5
Thinning factor	β	0.1	0.1
Quantum efficiency	η	0.8	0.5
Temporal noise	n_{AT}	5 electrons	250 electrons
Corrected uniformity	U_c	0.25%	1%
Pixel dimension	ρ_{pix}	20 cm	20 cm
Effective dwell time	τ_d	32 msec	32 msec
Ground emissivity	ε	—	0.9
Thermal signal (rms)	σ_T	—	3°C
Reflectivity signal (rms)	σ_r	0.1	—
Signal-to-noise ratio*	σ_o/σ_n	33	10

* designates optical power ratio, equivalent to electrical voltage

sand kilometers, which carries a telescope having a 10% fill factor. The satellite is assumed to include both visible and infrared sensors; the pixel dimensions for both have been set to 20 cm, which is the diffraction-limited Nyquist sample size for the long-wavelength camera.

The computed signal-to-noise ratio of 33 for the visible sensor is likely to be adequate for most reconstruction algorithms intended to overcome the aberrations introduced by aperture thinning. The evaluation of the infrared system is somewhat less optimistic, because a signal-to-noise ratio of 10 has been found to be marginal for the particular three-petal design discussed in the main body of this article. It should be noted, however, that modest improvements in the collector design and sensor performance could improve this factor substantially.

REFERENCES

1. R.D. Hudson, Jr., *Infrared System Engineering*, John Wiley, New York (1969).
2. J.J. Otazo, E.W. Tung, and R.R. Parenti, "Digital Filters for Infrared Target Acquisition Sensors," *SPIE* **238**, 78 (1980).
3. M.J. Cantella, "Staring Sensor Systems," *Lincoln Laboratory Project Memorandum No. 96PM-0002* (23 September 1992).
4. W.L. Wolfe and G.Z. Zissis, eds., *The Infrared Handbook*, SPIE Optical Engineering Press, Bellingham, WA (1978).

RONALD R. PARENTI
is a staff member in the Laser and Sensor Applications group. He received a B.S. degree in physics from Bowling Green State University in Ohio and M.S. and Ph.D. degrees in physics from Carnegie Mellon University in Pittsburgh. His thesis research dealt with the development of infrared fluorescence techniques to monitor atmospheric pollution. He joined Lincoln Laboratory in 1974. For the past twelve years he has worked in the field of adaptive optics, and he has a particular interest in the application of adaptive optics techniques to astronomical telescopes. Ron has served on several internal committees and was the Division 5 representative on the Innovative Research Program Committee for five years. He is currently a member of the Advanced Concepts Committee.